

# Identifying Contact Distance Uncertainty in Whisker Sensing with Tapered, Flexible Whiskers

Teresa A. Kent<sup>1</sup>, Hannah Emmett<sup>2</sup>, Mahnoush Babaei<sup>3</sup>, Mitra J. Z. Hartmann<sup>4</sup>, Sarah Bergbreiter<sup>5</sup>

**Abstract**—Whisker-based tactile sensors have the potential to perform fast and accurate 3D mappings of the environment, complementing vision-based methods under conditions of glare, reflection, proximity, and occlusion. However, current algorithms for mapping with whiskers make assumptions about the conditions of contact, and these assumptions are not always valid and can cause significant sensing errors. Here we introduce a new whisker sensing system with a tapered, flexible whisker. The system provides inputs to two separate algorithms for estimating radial contact distance on a whisker. Using a Gradient-Moment (GM) algorithm, we correctly detect contact distance in most cases (within 4% of the whisker length). We introduce the Z-Dissimilarity score as a new metric that quantifies uncertainty in the radial contact distance estimate using both the GM algorithm and a Moment-Force (MF) algorithm that exploits the tapered whisker design. Combining the two algorithms ultimately results in contact distance estimates more robust than either algorithm alone.

## I. INTRODUCTION

Many rodents navigate dark spaces using rhythmic protraction and retraction of their whiskers, a behavior called “whisking.” The ability to navigate and develop a three-dimensional (3D) map even in darkness [1], [2], [3] has inspired engineered whisker arrays that can do the same. The most effective whisker arrays can identify the contact point along the whisker’s length to create 3D scene maps [2]. In application, such arrays have mapped the fine details of a 3D face model [4], classified objects [5], defined shapes [6], [7], [8] and performed SLAM in a 3D scene [3].

In three dimensions, a contact point on a whisker is most easily defined by three components: radial contact distance ( $r$ ), the direction of bending (or rotation in the case of a rigid whisker), and the magnitude of bending (Fig. 1) [9]. Estimating radial contact distance is of particular importance to whisker mapping and at least nine separate algorithms have been described in the literature to localize contact to within 10% of whisker length accurately [10], [11]. However, all of these algorithms make assumptions about contact, ultimately limiting their application. For example,

\*This work was supported by NSF grant BCS-1921251 and MURI award number FA9550-19-1-0386

<sup>1</sup>Teresa Kent is a PhD student in the Robotics Institute, Carnegie Mellon University, 5000 Forbes Ave, Pittsburgh, PA, USA [tkent@andrew.cmu.edu](mailto:tkent@andrew.cmu.edu)

<sup>2</sup>Hannah Emmett contributed to this work while a PhD candidate in Mechanical Engineering at Northwestern University, Evanston, IL, USA

<sup>3</sup>Mahnoush Babaei is a research associate at the University of Texas Austin, Austin TX, USA

<sup>4</sup>Mitra J. Z. Hartmann is a Professor of Biomedical Engineering and Mechanical Engineering at Northwestern University, Evanston, IL, USA

<sup>5</sup>Sarah Bergbreiter is a Professor of Mechanical Engineering at Carnegie Mellon University, Pittsburgh, PA, USA

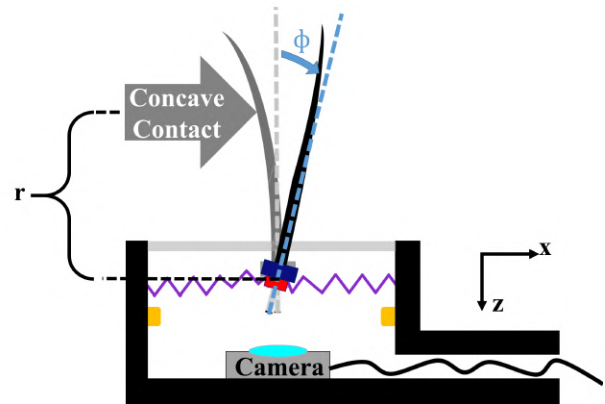


Fig. 1. A 3D contact point on the whisker is defined by three components: **Radial Contact Distance** ( $r$ ), defined in this paper as the distance in the  $z$ -direction from the point of rotation, **Direction of Bending** and **Magnitude of Bending** (rotation in the case of a rigid whisker). The algorithms discussed in this paper use three primary inputs to estimate  $r$ : 1.  $\Delta x$ , The distance the whisker has traveled in the  $x$ -direction since first contact occurred, 2.  $\phi$ , angular rotation around the base of the whisker, and 3.  $\delta z$ , downward motion of the whisker base caused by bending of a flexible whisker.

seven of the nine methods are only accurate under small-angle conditions, typically less than  $10^\circ$ - $14^\circ$ . Six of the nine methods obtain only a single contact point per whisk, and five of the nine require the user to know how the base of the whisker is moving (e.g., by using a motor encoder). These limitations increase the probability of undetected sensing failures. Many of the approaches also implicitly place strong constraints on allowed whisker motions, making mapping more challenging. In the present work, we demonstrate how using multiple algorithms together improves radial contact distance estimation.

The first algorithm is similar to two rotation-based algorithms: the Gradient-Moment (GM) algorithm [4], [12] and the sweeping method [13]. These algorithms use motion (either translation, rotation, or both) of the whisker base (e.g., a linear displacement,  $\Delta x$ ) along with a measurement of the whisker bending,  $\phi$ , to estimate the radial contact distance,  $r$  (Fig. 1). However, because this method depends on signal rates of change, it fails if the contact is made on a surface that deforms or moves (e.g., a leaf or a marble) as well as when the whisker translates parallel to a flat surface such as a wall [14]. In this second case, the whisker bending ( $\phi$ ) will stabilize at a fixed value in slipping contact with the wall despite the robot’s continued translation ( $\Delta x$ ), leading to a continually increasing estimate for  $r$ .

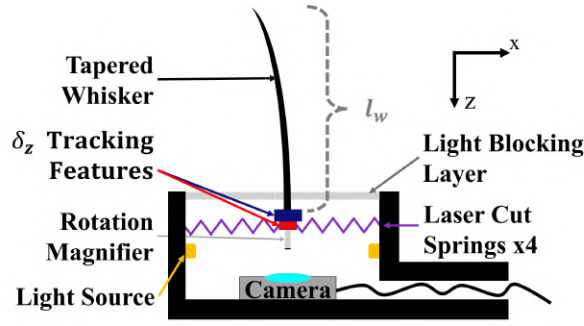


Fig. 2. A diagram of the whisker sensor. A tapered, flexible whisker is suspended over a camera using a laser-cut spring suspension. Tracking squares and rotation magnifiers amplify motions at the whisker base in the camera image.

A second method for radial contact point determination does not rely on knowledge of whisker motion. This method uses only mechanical signals at the whisker base (i.e., forces and moments), and can therefore provide accurate measurements even in the failure cases described above [10], [9]. We call this approach the “Moment-Force” (MF) algorithm because it relies on these two mechanical variables [9]. Unlike the GM method, in which the whiskers can be rigid and/or cylindrical, the MF approach requires a flexible whisker with taper [9]. As the whisker bends against an object, the whisker’s taper ensures that changes in the mechanical signals at the whisker base uniquely represent each 3D contact point. In previous work, some of the present authors used a whisker sensor with four strain gauges at the base to demonstrate success of the MF approach [15]. However, this previous work faced challenges with both the sensing system hardware (e.g., measurement drift and strain gauge attachment) as well as lower precision contact estimations.

In the present work, we describe a novel whisker sensor design with a flexible, tapered whisker that collects inputs for both the GM and MF algorithms. Inspired by previous camera-based whisker sensors [16], [17], we designed a whisker base that simplifies estimates of mN axial force and rotational moments as monitored by a camera. For this study, we focus only on the magnitude of the bending moment to estimate radial contact distance, and not the direction of bending. Bending direction will ultimately be required to create 3D maps. Using this sensing system, we make two contributions to the whisker-sensor literature. First, we quantify tradeoffs between the two algorithms (GM and MF) for estimated radial contact distance accuracy and precision during rigid contact, compliant contact, and slipping contact. Second, we introduce a new metric for whisker sensing, the “Z-Dissimilarity score,” which quantifies uncertainty in the radial contact distance estimate. This uncertainty estimate is based on the two separate estimates for  $r$  from the two separate algorithms. By combining the novel sensor with the two-algorithm approach, we generate accurate radial contact distance estimates with a confidence metric that can be used to identify GM-method failure cases.

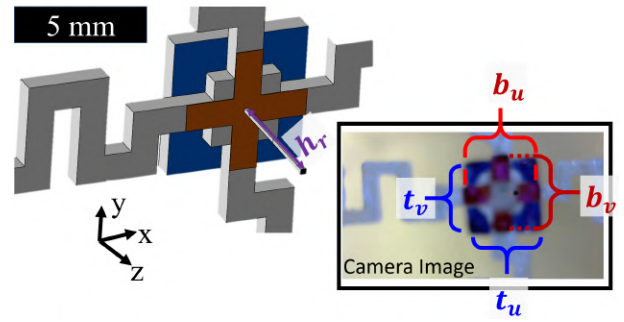


Fig. 3. There are three features used for vision-based tracking: the top tracking square (blue), the laser cut spring (gray), and the 3D-printed red cross with a 7.5 mm rotation magnifying rod extending toward the camera. In the camera image the widths and thicknesses of the  $\delta_z$  tracking features ( $b_u, b_v, t_u, t_v$ ) are used to calculate  $\delta_z$ .

## II. METHODS

### A. Sensing System Manufacturing and Design

1) *Sensing Hardware*: Fig. 2 shows a diagram of the whisker sensing system. Four 0.75 mm thick laser-cut acrylic serpentine springs suspend the whisker 25 mm above the camera (Logitech HD Webcam C310). 3D-printed tracking features are glued to the acrylic springs. A 3D-printed housing fixes the camera and springs in place. Six LEDs (Micro Litz Pure White) and a white cloth taped over the springs improve lighting consistency between frames. Two types of whiskers are used for experiments. The first is a rigid, 1 mm-diameter carbon fiber rod. The second is a 150 mm long tapered, flexible whisker that was manufactured using the conforming fiber drawing process on a piece of filament as described in [18].

The tracking features in Fig. 3 were chosen to simplify estimation of the whisker magnitude of rotation,  $\phi$ , and axial deflection,  $\delta_z$ , in camera images as seen in Fig. 4. The  $\delta_z$  tracking features include two components approximately equidistant from the spring’s center of rotation: a blue acrylic square and a red cross. To provide improved estimates of  $\phi$ , the cross is printed with a 7.5 mm long rotation magnifier extending down toward the camera. The tip of the rotation magnifier is painted black.

2) *Sensing Software*: Motion of the whisker is captured by monitoring the tracking features with a camera, as shown in Fig. 4. Each image frame is white balanced, and a Lucas-Kanade translation-only template-updating tracking algorithm is used to quantify movement of the  $\delta_z$  tracking features [19]. To amplify red and blue contrast and convert the image into each channel, each pixel is assigned a new color ( $G$ ) by comparing each pixel’s red ( $R$ ) and blue ( $B$ ) components to the average color value of the pixel ( $\bar{P}$ ).

$$G = \frac{(B - \bar{P}) - (R - \bar{P})}{\bar{P}} \quad (1)$$

The tracked points are the cross’ outermost edges and the square’s corners. A color-based segmentation algorithm tracks the tip of the rotation magnifier. Tracking code can be found at [20].

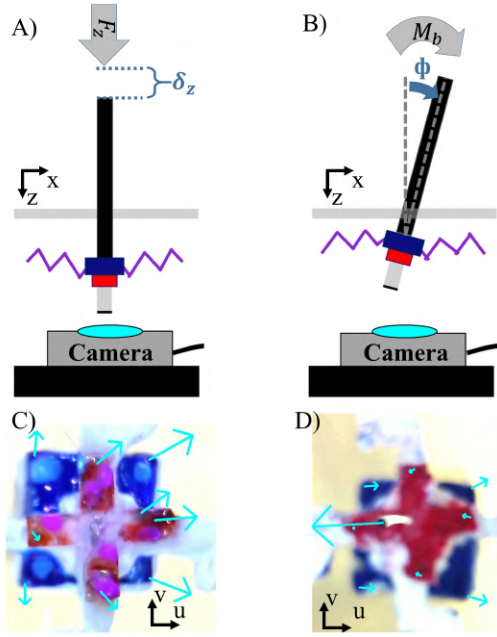


Fig. 4. The global motions of the sensing system (A, B) affect the camera images (C, D). A downward deflection caused by an axial force,  $F_z$ , (A) brings the tracking squares and rod closer to the camera, causing the apparent areas of the square and the cross to increase (C).  $\phi$  rotations, caused by a bending moment,  $M_b$ , (B) cause translations of the rotation magnifier (D). The cyan arrows are added during tracking and represent 10x the detected motion in pixels.

### B. Calculating Deflections and Rotations

We solve for two signals from the camera image: the axial deflection,  $\delta_z$  (Fig. 4A) and rotation magnitude,  $\phi$  (Fig. 4B). As noted previously, the direction of the rotation,  $\theta$ , can also be calculated from this image [16], but is not studied here. When a positive z-deflection occurs, the system moves closer to the camera. This motion affects all tracked points equally (Fig. 4C). It is therefore vital to remove the effect of  $\delta_z$  before solving for  $\phi$  rotation.  $\delta_z$  can be calculated using the initial and current values for the projected widths ( $b_u$ ,  $b_v$ ) and thicknesses ( $t_u$ ,  $t_v$ ) of the tracking features (Fig. 3). In equation 2, only one of these variables is used, but any can be substituted. The subscript  $i$  represents the initial calibration frame and  $n$  represents the current frame.  $z_i$  is the initial distance between the camera and the tracked object (25 mm).

$$\delta_{zn} = z_i * \left(1 - \frac{b_{ui}}{b_{un}}\right) \quad (2)$$

Axial deflection also translates the rotation magnifier rod in the camera frame.  $\Delta c_u$  and  $\Delta c_v$  represent the rod tip's pixel translation in the horizontal and vertical directions.

$$\Delta c_u = \frac{(z_i - h_r) * c_{ui}}{(z_i - h_r) - \delta_z} - c_{ui} \quad (3)$$

$$\Delta c_v = \frac{(z_i - h_r) * c_{vi}}{(z_i - h_r) - \delta_z} - c_{vi} \quad (4)$$

The  $\phi$  rotation primarily affects the rotation magnifying rod (Fig. 4D). The effects of  $\delta_z$  translation (equations 3 and 4) are removed from the change in displacement of the rod

in the camera frame ( $\delta_u$ ,  $\delta_v$ ) before solving for  $\phi_n$ . Variables used are provided in Table I.

$$\mu = \frac{z_i - h_r}{u_{res}} \tan(u_{aov}) / \frac{z_i - h_r}{v_{res}} \tan(v_{aov}) \quad (5)$$

$$\rho = \frac{1}{2} \left( \frac{z_i - h_r}{u_{res}} \tan(u_{aov}) + \frac{z_i - h_r}{v_{res}} \tan(v_{aov}) \right) \quad (6)$$

$$\phi_n = \arctan \left( \rho \frac{\sqrt{\delta_{un}^2 + (\delta_{vn} * \mu)^2}}{h_r} \right) \quad (7)$$

### C. Estimating moments and forces from $\phi$ and $\delta_z$

Similar to previous work [21], our design can convert the rotations and deflections of the whisker base into forces and moments using the equations from [22]. In the MF method, the precision of estimated radial contact distance will depend strongly on the minimum detectable axial force [15]. For example, for the whisker used on our sensor, the quasistatic simulations of Huet et al. [9] estimate a difference in  $F_z$  force of just 1.8 mN between contact points separated by only 1 cm after a 10° rotation. Developing a sensor with such a small detectable force is challenging. In order to make informed design decisions about the parameters in our final design (Table I) we had to use not only the anticipated forces and moments from the quasistatic simulations, but also the springs' response to those forces and moments [22], and the equations for pixel density of the camera (equation 6). Scripts to model these designs can be found at [20].

Predicting moments and forces from  $\phi$  and  $\delta_z$  is useful for design of the physical whisker sensing system, but it should be noted that the algorithms described below, calculated moments and forces were not used. As described in the results, the springs stayed in a linear regime. Therefore a linear relationship exists between bending moment and  $\phi$  as well as between axial force and  $\delta_z$ . These results were similar to those found in previous work in [21], [15].

TABLE I  
DESIGN PARAMETERS

Parameter	Variable	Value
spring pitch	$p$	2.6 mm
spring length	$l$	1.5 mm
spring width	$w$	0.75 mm
spring thickness	$t$	0.75 mm
number of spring turns	$n$	12
square magnifier width /thickness	$t_w/t_t$	5 mm
cross magnifier width /thickness	$b_w/b_t$	4 mm
rod height	$h_r$	7.5 mm
v/u corrector	$\mu$	1.02
u resolution	$u_{res}$	1280 pixels
v resolution	$v_{res}$	720 pixels
u angle of view	$u_{aov}$	26.95 °
v angle of view	$v_{aov}$	16.26 °
springs offset from camera	$z_i$	25.0 mm

### D. Algorithms to Estimate Radial Contact

The primary goal of this work is to combine the Gradient-Moment (GM) and Moment-Force (MF) algorithms so as to improve radial contact distance estimates, and to provide a metric that describes the estimates combined uncertainty.



1) *Gradient-Moment (GM) Algorithm*: The GM algorithm provides an estimate of radial contact distance (denoted as  $\hat{r}_{GM}$  to distinguish it from the actual distance,  $r$ ) based on the whisker rotation,  $\phi$ , and the motion at the whisker base (in this case a linear translation,  $\Delta x$ ).

$$\hat{r}_{GM} = \frac{C \frac{\Delta x}{\phi} l_w}{l_w + C \frac{\Delta x}{\phi}} \quad (8)$$

In equation 8,  $l_w$  is the length of the whisker (150 mm) and  $C$  is a constant related to the whisker stiffness. The value of  $C$  can be experimentally estimated by comparing  $\phi$  and  $\Delta x$ . Given the system's small minimum detectable moment (0.025 N – mm) we expect this method to provide relatively precise estimates of contact distance. Worth noting, in some previous work,  $\dot{x}$  and  $\dot{\phi}$  are used to solve for  $\hat{r}$  instead [4].

2) *Moment-Force (MF) Algorithm*: This algorithm uses  $\phi$  and  $\delta_z$ , which are linearly proportional to the bending moment and the axial force, to estimate radial contact distance  $\hat{r}_{MF}$ . In this case, a simple analytical mapping between variables does not exist, therefore previous work has used look-up tables and classification methods to predict  $\hat{r}_{MF}$  [9], [15]. In the present work, we use a k-nearest neighbor approach to estimate  $\hat{r}_{MF}$ .

$$d_k = \frac{\phi - \phi_k}{35} + \frac{\delta_z - \delta_{zk}}{1} \quad (9)$$

$$\hat{r}_{MF} = \frac{\sum_{k=1}^7 r/d_k}{\sum_{k=1}^7 1/d_k} \quad (10)$$

In equations 9 and 10,  $r$  represents the true label of one of the ( $k = 7$ ) closest points to the new sensor value. Equation 9 calculates the distance between a point in the training set ( $\phi_k, \delta_{zk}$ ) and the current sensed point ( $\phi, \delta_z$ ). These values are then divided by a normalizing value of  $35^\circ$  and 1 mm, which represent the maximum expected values of  $\phi$  and  $\delta_z$  respectively. Given that the precision of this estimate relies on the minimum detectable force, we expect this method to yield lower precision estimates than the GM approach. However, the MF approach should remain accurate in cases where GM might fail (e.g., compliant or slipping contact).

3) *Z-Dissimilarity Score*: In statistics, Z-scores typically provide a measure of distance from the mean. We generated a Z-Dissimilarity score to provide a metric of uncertainty in the  $\hat{r}_{GM}$  estimate. The score is calculated in two steps. First, we compute the (signed) difference between the values of  $r$  predicted by the two different estimation methods. This difference is then normalized by the expected standard deviation of  $\hat{r}_{GM}$  at the relevant value of  $\phi$ .

$$Z(r = \hat{r}_{GM}) = \frac{\hat{r}_{GM} - \hat{r}_{MF}}{\sigma_{r_{GM}}(\phi)} \quad (11)$$

A value of  $Z$  below 0.5 indicates an expected deviation while values over 1.0 indicate a probable error.

4) *Shape Reconstruction*: To demonstrate success of the present approach, we attempt to reconstruct 2D shapes using the estimated radial contact distance,  $\hat{r}$ , and linear translation of the whisker base,  $x$ . The estimated contact location in

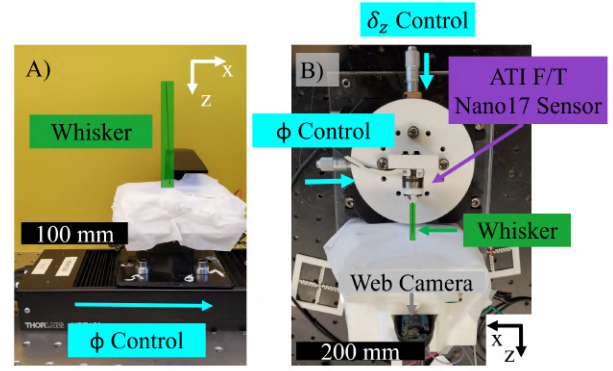


Fig. 5. **Experimental test setups**: A) A rigid (shown) and flexible whisker were translated relative to a 3D printed rigid surface by a motorized linear stage. B) Using a manual linear stage  $\delta_z$  deflections could be applied with a precision of 0.05 mm, while a force-torque sensor measured the force applied to the spring system.

the x-direction is provided below. The sign depends on the direction of travel of the whisker.

$$\hat{x} = x \pm \hat{r} \sin \phi \quad (12)$$

#### E. Experimental Setup

To calibrate the sensing system, a 1 mm diameter rigid whisker was glued to the spring suspension and attached to a ThorLabs NRT-150 motorized linear stage as seen in Fig. 5A. Using the linear stage, the whisker base was moved in 1 mm increments along the x-axis to rotate the whisker between  $0^\circ$  to  $18^\circ$  to test the accuracy of  $\phi$  calculations. Data were collected over two separate trials.

In a second test, we used a ThorLabs manual linear stage with an attached 6-axis force-torque sensor (ATI Nano17) to apply displacements to the tip of the rigid whisker (Fig. 5B).  $\phi$  and  $\delta_z$  were calculated from camera images and were correlated with the the applied  $M_x$  and  $F_z$  as measured by the force-torque sensor. This setup allowed us to test both the accuracy of the  $\delta_z$  calculations and confirm that  $F_z$  and  $\delta_z$  were linearly related.

In our third test, a tapered, flexible whisker was attached to a spring suspension system identical to that used in the first two tests. Contact was applied at varying radial contact distances using the motorized linear stage from Test 1. Contact was first applied with a rigid 3D printed surface at radial contact distances of [22.5, 27.5, 33.5, 42.5, 50, 60, 72.5, 90] mm. The linear stage controlled the position of the whisker base in the x-direction was stepped in 1 mm increments with 1 s pauses between steps. In separate tests, contact was applied using a highly-compliant object (a thin pipe cleaner) at radial contact distances of [35, 55, 90] mm. In our final test, we slid the same tapered, flexible whisker across cross-sections of a water bottle (circular) and a box (L-shaped).

All tests were run assuming a quasi-static whisker. All data were collected during pauses of the linear stages used

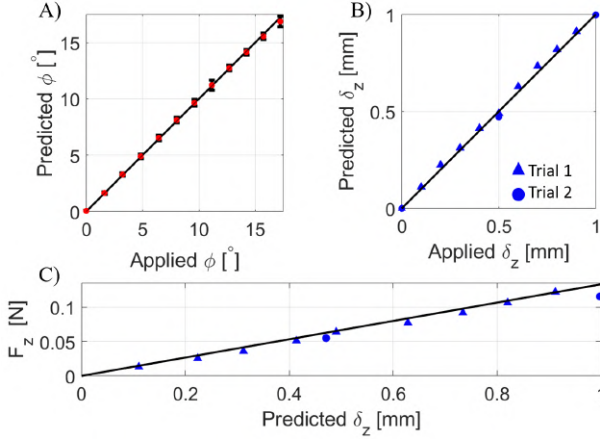


Fig. 6. A) The accuracy of predicted  $\phi$  is compared with applied  $\phi$  over 18 trials. Error bars represent standard deviations. B) The accuracy of predicted  $\delta_z$  is compared with applied  $\delta_z$  over two trials. C) From the same test as B. The accuracy of predicted  $F_z$  from the whisker sensor is compared with the value of  $F_z$  measured by the force-torque sensor. The black line represents the expected  $F_z$  for a  $\delta_z$  deflection by the spring model. [22]

for whisker motion or pauses in application of forces. We ensured at least one second between steps. Each data point in the results represents the median of calculated  $\phi$  and  $\delta_z$  during these pauses. Example video recordings of each test can be found in the supplemental video.

### III. RESULTS AND DISCUSSION

#### A. Accuracy of $\phi$ , $\delta_z$ , and $F_z$

A comparison between applied and predicted values of  $\phi$ ,  $\delta_z$ , and  $F_z$  are presented in Fig. 6. Root mean square error (RMSE) is calculated for each measurement. RMSE of  $\phi$  is  $0.31^\circ$  without correcting for the axial deflection, and improves to  $0.22^\circ$  when  $\delta_z$  is removed using Eqns. 3 and 4. These results are more precise than those obtained with the previous version of the sensor hardware [16]. RMSE of  $\delta_z$  and  $F_z$  are  $0.04\text{ mm}$  and  $2\text{ mN}$  over a  $0\text{ mm}$  to  $1\text{ mm}$   $\delta_z$  deflection. The expected range for deflection is calculated from quasi-static simulations and spring models [9], [22]).

#### B. Radial Contact Distance with Rigid Contact

The Gradient-Moment (GM) algorithm provides an analytical estimate of  $\hat{r}$  given the lateral distance traveled at the whisker base,  $\Delta x$ , and the estimated  $\phi$  as calculated in Eqn. 8. Using the experimental data collected from the various contact heights shown in Fig. 7A, the best fit for constant  $C$  in Eqn. 8 was found to be 132. Accuracy and precision of this method can be quantified by examining the error in radial contact distance,  $r - \hat{r}_{GM}$ . The mean ( $\mu_{GM}$ ) and standard deviation ( $\sigma_{GM}$ ) of this error across all data in Fig. 7A is presented in Table II. The values in this table were obtained at varying ranges of  $\phi$ ; precision is often shown to improve as  $\phi$  increases in previous applications of the MF and sweeping method algorithms [15], [13]. The GM algorithm represents an accurate measurement with high precision given the mean

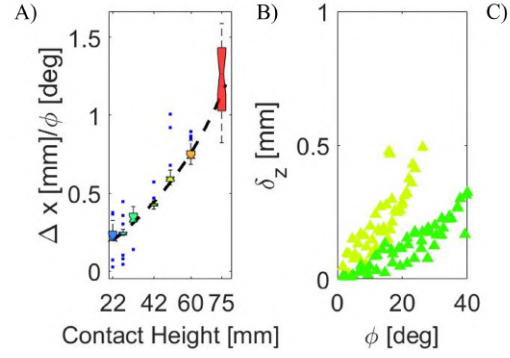


Fig. 7. Values for  $\phi$ ,  $\delta_z$ , and applied translation  $\Delta x$  were collected for the flexible whisker against a rigid contact at seven contact heights. A) The model in equation 8 is plotted against box plots, illustrating the distributions of the experimental data. The applied  $r$  values and experimentally measured  $\frac{\Delta x}{\phi}$  were used to estimate constant  $C$ . Each box plot had a minimum of 18 data points. B) The MF algorithm uses classification on the  $\phi$  vs  $\delta_z$  graph to identify radial contact height. Example data from two applied  $r$  values (42 mm and 50 mm) are plotted here. C) The applied contact distances relative to  $l_w$ .

close to zero and a standard deviation of approximately  $3\text{ mm}$  across a range of  $\phi$  values.

Because the MF algorithm uses a classification approach to estimate  $\hat{r}_{MF}$ , experimental data should show separation between data collected at different applied contact distances in  $(\phi, \delta_z)$  space. To avoid cluttering, Fig. 7B shows only two applied contact distances, corresponding to  $42\text{ mm}$  and  $50\text{ mm}$ . These two distances show clear separation, especially at larger values of  $\phi$ . Similar to the GM results,  $\mu_{MF}$  and  $\sigma_{MF}$  are calculated for the error in radial contact distance estimates for the MF approach,  $r - \hat{r}_{MF}$ , and presented in Table II. Both the accuracy and precision of  $\hat{r}_{MF}$  improve as  $\phi$  increases, but the MF algorithm is clearly outperformed by GM in this case of rigid contact.

TABLE II  
DISTANCE ERROR  $r - \hat{r}$  [MM] ON A RIGID SURFACE

$\phi <$	$\mu_{GM}$	$\sigma_{GM}$	$\mu_{MF}$	$\sigma_{MF}$
$2.5^\circ$	0.5	3.2	0.6	20.3
$5^\circ$	0.5	3.1	0.5	19.4
$10^\circ$	0.4	3.1	0.7	17.4
$20^\circ$	-0.3	2.8	0.2	13.3

#### C. Radial Contact Distance with Compliant Contact

Contact with the pipe cleaner is an expected failure mode for the GM algorithm because the pipe cleaner bends during contact. The GM algorithm overestimates  $\hat{r}$  when contacting a compliant surface because the whisker bends less than expected. This expected result is borne out in the large negative values for the means of the radial contact distance error ( $\mu_{GM}$ ) presented in Table III. The MF algorithm accuracy outperforms the GM algorithm on a compliant surface, but precision (represented by  $\sigma_{MF}$ ) remains poor in comparison to the GM method. Data from experimental measurements summarized in Tables II and III are also presented using box and whisker plots in Fig. 8.

TABLE III  
DISTANCE ERROR  $r - \hat{r}$  [MM] ON A COMPLIANT SURFACE

$\phi <$	$\mu_{GM}$	$\sigma_{GM}$	$\mu_{MF}$	$\sigma_{MF}$
$2.5^\circ$	-23.5	8.2	7.4	24.6
$5^\circ$	-23.5	8.2	4.6	24.2
$7.5^\circ$	-23.6	8.3	0.9	22.6
$10^\circ$	-23.1	1.1	-3.5	19.6

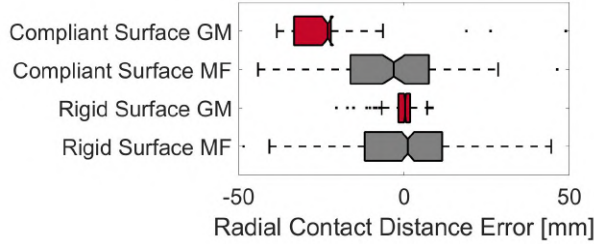


Fig. 8. Boxplots of the error in radial contact distance estimation  $r - \hat{r}$  using the GM and MF algorithms are compared on both compliant and rigid surfaces.

#### D. Z-Dissimilarity Score

We tested the Z-Dissimilarity score defined in Eqn. 11 on the data collected from rigid contact, compliant contact and the shape reconstruction task. Because the goal of the Z-Dissimilarity score is to identify times of incorrect prediction, we compared the Z-Dissimilarity scores with errors in radial contact distance estimation (e.g.,  $r - \hat{r}_{GM}$ ). A Z value above 1 indicates that the difference between the two  $\hat{r}$  estimates is not likely to be explained by the standard deviation. When  $r - \hat{r}_{GM} > 15$  mm, the Z-Dissimilarity score was greater than 1.0 for 82% of the compliant contact and rigid contact data and greater than 0.5 for 94% of the data. In contrast, when  $r - \hat{r}_{GM} < 15$  mm, the Z-Dissimilarity score was greater than 1.0 for 26% of the data and greater than 0.5 for 36% of the data. Although not a perfect measure of uncertainty, the Z-Dissimilarity score is a strong indicator of instances when more data might be needed to improve the estimate of radial contact distance.

A shape reconstruction task provides a graphical indication of Z-Dissimilarity score as shown in Fig. 9. Sliding along a surface represents a second common failure mode for radial contact distance estimation. Upon initial contact, the GM algorithm is more precise and accurate as it traces the cube and cylinder shapes. However, as the translation increased and the gradient of the surfaces decreased, the whisker began to slip; during slip, the MF method maintained its accuracy while the GM method lost accuracy, and the Z-Dissimilarity score increased as indicated by the heatmap colors in Fig. 9.

#### IV. CONCLUSION

In this work we demonstrated a new whisker sensor system design that can sense the information required to implement two algorithms for radial contact distance estimation: Gradient-Moment (GM) and Moment-Force (MF). Using this sensor, we measured accuracy and precision for both methods and demonstrated that the GM algorithm

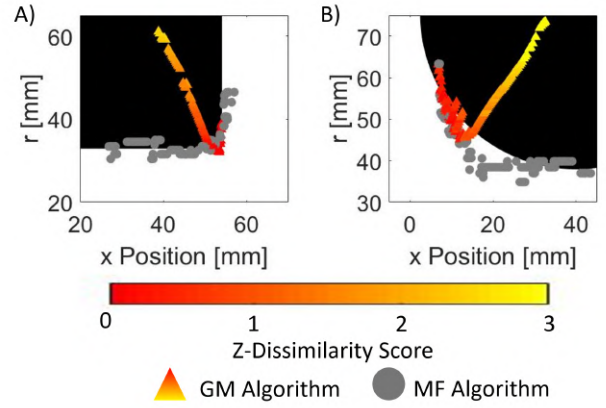


Fig. 9. A linear stage swept the whisker across a box (left) and the circular cross-section of a water bottle (right) while data were collected from the sensor. Radial contact estimates from the GM algorithm (red/yellow) and the MF algorithm (gray) are compared. The GM algorithm can accurately and precisely localize the contact point until the whisker begins to slip, at which point the accuracy decreases significantly. The MF algorithm is less precise but remains accurate during slip. The Z-Dissimilarity score determines the color of each point plotted for the GM algorithm.

does not accurately estimate radial contact distance during compliant contact and contact with slip. We introduced a Z-Dissimilarity score that can indicate these failure modes and showed that the MF algorithm can provide an accurate, albeit noisy, contact distance estimate when the GM algorithm fails.

The whisker sensing system in this paper relies on a few key assumptions:

- 1) We estimate radial contact distance only when the whisker is in quasi-static conditions
- 2) We assume the whisker makes contact with only one object at a given time.
- 3) We assume all GM failure cases result from a reduced bend of the whisker. This assumption fails if an object moving towards the whisker.
- 4) We did not examine the direction of whisker bending.

Addressing these assumptions provides several avenues for future work.

It should be noted that our sensor generates predictions that are as precise as other MF sensors [15], but performs considerably worse than the GM algorithm in cases of contact with a rigid object, due to poor resolution in  $\delta_z$ . Non-slipping, rigid contact can be used for many applications and the  $\hat{r}_{GM}$  estimate is a simple equation. Applying  $\hat{r}_{GM}$  with our Z-Dissimilarity score could allow robots with whiskers to traverse space quickly, only slowing down when the robot predicts a more difficult mapping. The score allows researchers to remove data points above a threshold, incorporate the uncertainty into the mappings based on task requirements, or switch to the MF algorithm. The algorithm could also potentially help the robot determine when to make a whisk, i.e., when to reset the sensor in space. Combining multiple sensing algorithms can also have other benefits for whisker sensing. For example, the combination could be used to map surface compliance as suggested in [9] or to increase accuracy and precision during tapping contact [23], [24].

## REFERENCES

- [1] R. A. Russell, "Using tactile whiskers to measure surface contours," in *Proceedings 1992 IEEE International Conference on Robotics and Automation*. IEEE Computer Society, 1992, pp. 1295–1296.
- [2] C. W. Fox and T. J. Prescott, "Mapping with sparse local sensors and strong hierarchical priors," in *Conference Towards Autonomous Robotic Systems*. Springer, 2011, pp. 183–194.
- [3] M. Salman and M. J. Pearson, "Whisker-ratslam applied to 6d object identification and spatial localisation," in *Conference on Biomimetic and Biohybrid Systems*. Springer, 2018, pp. 403–414.
- [4] J. H. Solomon and M. J. Hartmann, "Robotic whiskers used to sense features," *Nature*, vol. 443, no. 7111, pp. 525–525, 2006.
- [5] C. Xiao, S. Xu, W. Wu, and J. Wachs, "Active multi-object exploration and recognition via tactile whiskers," *arXiv preprint arXiv:2109.03976*, 2021.
- [6] D. Kim and R. Möller, "Biomimetic whiskers for shape recognition," *Robotics and Autonomous Systems*, vol. 55, no. 3, pp. 229–243, 2007.
- [7] J. F. Wilson and Z. Chen, "A whisker probe system for shape perception of solids," 1995.
- [8] G. R. Scholz and C. D. Rahn, "Profile sensing with an actuated whisker," *IEEE Transactions on Robotics and Automation*, vol. 20, no. 1, pp. 124–127, 2004.
- [9] L. A. Huet, J. W. Rudnicki, and M. J. Hartmann, "Tactile sensing with whiskers of various shapes: Determining the three-dimensional location of object contact based on mechanical signals at the whisker base," *Soft robotics*, vol. 4, no. 2, pp. 88–102, 2017.
- [10] J. H. Solomon and M. J. Hartmann, "Radial distance determination in the rat vibrissal system and the effects of weber's law," *Philosophical Transactions of the Royal Society B: Biological Sciences*, vol. 366, no. 1581, pp. 3049–3057, 2011.
- [11] N. H. Nguyen, T. D. Ngo, D. Q. Nguyen, *et al.*, "Contact distance estimation by a soft active whisker sensor based on morphological computation," in *2020 8th IEEE RAS/EMBS International Conference for Biomedical Robotics and Biomechatronics (BioRob)*. IEEE, 2020, pp. 322–327.
- [12] C. W. Fox, M. H. Evans, M. J. Pearson, and T. J. Prescott, "Towards hierarchical blackboard mapping on a whiskered robot," *Robotics and Autonomous Systems*, vol. 60, no. 11, pp. 1356–1366, 2012.
- [13] J. H. Solomon and M. J. Hartmann, "Extracting object contours with the sweep of a robotic whisker using torque information," *The International Journal of Robotics Research*, vol. 29, no. 9, pp. 1233–1245, 2010.
- [14] M. Kaneko, N. Kanayama, and T. Tsuji, "Active antenna for contact sensing," *IEEE Transactions on robotics and automation*, vol. 14, no. 2, pp. 278–291, 1998.
- [15] H. M. Emmett, M. M. Graff, and M. J. Hartmann, "A novel whisker sensor used for 3d contact point determination and contour extraction," in *Robotics: science and systems*, 2018.
- [16] T. A. Kent, S. Kim, G. Kornilowicz, W. Yuan, M. J. Hartmann, and S. Bergbreiter, "Whisksight: A reconfigurable, vision-based, optical whisker sensing array for simultaneous contact, airflow, and inertia stimulus detection," *IEEE Robotics and Automation Letters*, vol. 6, no. 2, pp. 3357–3364, 2021.
- [17] N. F. Lepora, M. Pearson, and L. Cramphorn, "Tacwhiskers: Biomimetic optical tactile whiskered robots," in *2018 IEEE/RSJ International Conference on Intelligent Robots and Systems (IROS)*. IEEE, 2018, pp. 7628–7634.
- [18] D. W. Collinson, H. M. Emmett, J. Ning, M. J. Hartmann, and L. C. Brinson, "Tapered polymer whiskers to enable three-dimensional tactile feature extraction," *Soft Robotics*, vol. 8, no. 1, pp. 44–58, 2021.
- [19] S. Baker and I. Matthews, "Lucas-kanade 20 years on: A unifying framework," *International journal of computer vision*, vol. 56, no. 3, pp. 221–255, 2004.
- [20] T. Kent, "Identifying-contact-distance-uncertainty-in-whisker-sensing-with-tapered-flexible-whiskers," <https://github.com/TeresaAKent/Identifying-Contact-Distance-Uncertainty-in-Whisker-Sensing-with-Tapered-Flexible-Whiskers.git>, 2022.
- [21] S. Kim, C. Velez, D. K. Patel, and S. Bergbreiter, "A magnetically transduced whisker for angular displacement and moment sensing," in *2019 IEEE/RSJ International Conference on Intelligent Robots and Systems (IROS)*. IEEE, 2019, pp. 665–671.
- [22] G. Barillaro, A. Molfese, A. Nannini, and F. Pieri, "Analysis, simulation and relative performances of two kinds of serpentine springs," *Journal of Micromechanics and Microengineering*, vol. 15, no. 4, p. 736, 2005.
- [23] L. Mérida-Calvo, D. Feliu-Talegón, and V. Feliu-Batlle, "Improving the detection of the contact point in active sensing antennae by processing combined static and dynamic information," *Sensors*, vol. 21, no. 5, p. 1808, 2021.
- [24] M. Evans, C. W. Fox, M. J. Pearson, N. F. Lepora, and T. J. Prescott, "Whisker-object contact speed affects radial distance estimation," in *2010 IEEE International Conference on Robotics and Biomimetics*. IEEE, 2010, pp. 720–725.